


 Cite this: *RSC Adv.*, 2020, 10, 34323

# Solid-state synthesis of few-layer cobalt-doped MoS<sub>2</sub> with CoMoS phase on nitrogen-doped graphene driven by microwave irradiation for hydrogen electrocatalysis†

 Junpeng Fan,<sup>a</sup> Joakim Ekspong,<sup>a</sup> Anumol Ashok,<sup>b</sup> Sergey Koroidov<sup>c</sup> and Eduardo Gracia-Espino<sup>\*,a</sup>

The high catalytic activity of cobalt-doped MoS<sub>2</sub> (Co–MoS<sub>2</sub>) observed in several chemical reactions such as hydrogen evolution and hydrodesulfurization, among others, is mainly attributed to the formation of the CoMoS phase, in which Co occupies the edge-sites of MoS<sub>2</sub>. Unfortunately, its production represents a challenge due to limited cobalt incorporation and considerable segregation into sulfides and sulfates. We, therefore, developed a fast and efficient solid-state microwave irradiation synthesis process suitable for producing thin Co–MoS<sub>2</sub> flakes (~3–8 layers) attached on nitrogen-doped reduced graphene oxide. The CoMoS phase is predominant in samples with up to 15 at% of cobalt, and only a slight segregation into cobalt sulfides/sulfates is noticed at larger Co content. The Co–MoS<sub>2</sub> flakes exhibit a large number of defects resulting in wavy sheets with significant variations in interlayer distance. The catalytic performance was investigated by evaluating the activity towards the hydrogen evolution reaction (HER), and a gradual improvement with increased amount of Co was observed, reaching a maximum at 15 at% with an overpotential of 197 mV at –10 mA cm<sup>–2</sup>, and a Tafel slope of 61 mV dec<sup>–1</sup>. The Co doping had little effect on the HER mechanism, but a reduced onset potential and charge transfer resistance contributed to the improved activity. Our results demonstrate the feasibility of using a rapid microwave irradiation process to produce highly doped Co–MoS<sub>2</sub> with predominant CoMoS phase, excellent HER activity, and operational stability.

 Received 25th June 2020  
Accepted 8th September 2020

DOI: 10.1039/d0ra05560c

[rsc.li/rsc-advances](http://rsc.li/rsc-advances)

## Introduction

Molybdenum disulfide, a layered transition metal dichalcogenide, is well recognized as a promising catalyst for several chemical and electrochemical processes, and its success relies on the possibility of tuning its intrinsic properties by phase, defect, and edge engineering.<sup>1–3</sup> In particular, the feasibility of incorporating diverse transition metals into the MoS<sub>2</sub> lattice has been a successful strategy to easily modify the overall catalytic performance, where in particular Co doping has shown the best performance for several reactions such as hydrogen evolution reaction (HER),<sup>4</sup> hydrodesulfurization (HDS),<sup>5,6</sup> carbon monoxide reduction,<sup>7</sup> and sodium-ion batteries,<sup>8</sup> among others. Cobalt incorporation into MoS<sub>2</sub> might occur as Co replacing Mo atoms along the MoS<sub>2</sub> lattice without a particular order, or as

a more peculiar arrangement where Co mainly occupies the edge-sites of MoS<sub>2</sub> flakes, in what is known as the CoMoS phase.<sup>9,10</sup> This phase is often observed at low cobalt doping, and it has been identified as the active phase/sites for both HER and HDS reactions,<sup>4–6</sup> while at large doping concentration there is often cobalt segregation into cobalt sulfides and sulfates, resulting in lower catalytic activity.<sup>9,10</sup> Therefore, incorporating Co atoms to form the CoMoS phase is critical for the activity of Co–MoS<sub>2</sub> catalysts, and thus several synthetic routes have been previously developed involving sulfidization of Co–Mo complex at high temperature under H<sub>2</sub>S stream,<sup>11</sup> annealing of amorphous Co-doped MoS<sub>2</sub> at a high temperatures,<sup>10</sup> incipient wetness impregnation,<sup>5</sup> electrodeposition,<sup>12</sup> and hydrothermal/solvothermal synthesis.<sup>6,13,14</sup> Generally, these methods required expensive or hazardous chemicals, high temperatures, and long reaction times. As an alternative process, solid-state synthesis using microwave irradiation can be used to speed up the production process. However, these methods have rarely been used to produce transition metal dichalcogenides, since most precursors interact weakly with microwaves, and thus a susceptor is needed to absorb electromagnetic radiation and convert it into heat.<sup>15–18</sup> Consequently, leading to high

<sup>a</sup>Department of Physics, Umeå University, Umeå 90187, Sweden. E-mail: [eduardo.gracia@umu.se](mailto:eduardo.gracia@umu.se)
<sup>b</sup>Department of Materials and Environmental Chemistry, Stockholm University, Stockholm 106 91, Sweden

<sup>c</sup>Department of Physics, Stockholm University, Stockholm 106 91, Sweden

† Electronic supplementary information (ESI) available. See DOI: 10.1039/d0ra05560c



temperatures with large heating rates, facilitating the pyrolysis and synthesis of target materials with high efficiency. Among microwave-absorbing materials, carbon-based materials with rich delocalized network of  $\pi$ -electrons (e.g. nanotubes and graphene) exhibit a rapid response to an alternating electromagnetic field giving rise to an electric current causing resistive heating in the material,<sup>19</sup> and thus localized high temperatures can be achieved in seconds. In addition, carbon nanomaterials act as excellent material support by facilitating the production of nanoparticulate structures, minimizing agglomeration, improving stability, and enhancing electron transport.<sup>20–23</sup>

We, therefore, exploit the ability of nanocarbons to easily absorb microwaves to develop a solid-state synthesis process driven by microwave irradiation to produce cobalt-doped edge-terminated layered  $\text{MoS}_2$  directly on nitrogen-doped reduced graphene oxide (N-rGO<sub>x</sub>). The as-produced Co– $\text{MoS}_2$  exhibited the CoMoS phase, and only a slight segregation to cobalt sulfides was observed at Co content above 15 at%. The Co– $\text{MoS}_2$  was tested as electrocatalyst towards the hydrogen evolution reaction achieving an overpotential of 197 mV at 10 mA cm<sup>-2</sup>, with excellent operational stability, in line with previous CoMoS electrocatalysts.

## Experimental section

### Materials

Graphite powder (100 mesh, 99.9995%) was purchased from Alfa Aesar. Orthophosphoric acid ( $\text{H}_3\text{PO}_4$ , 85%) was purchased from Fisher Scientific. Sulfuric acid ( $\text{H}_2\text{SO}_4$ , 95–97%), potassium permanganate ( $\text{KMnO}_4$ , 99%), molybdenum hexacarbonyl ( $\text{Mo}(\text{CO})_6$ , 98%), thiourea ( $\text{SC}(\text{NH}_2)_2$ , 99%) and cobalt nitrate hexahydrate ( $\text{Co}(\text{NO}_3)_2 \cdot 6\text{H}_2\text{O}$ , 98%) were purchased from Sigma-Aldrich. Pt@C (20 wt% on Vulcan) was acquired from Premetek. Absolute ethanol ( $\text{CH}_3\text{CH}_2\text{OH}$ , 99.96%) was purchased from VWR. All chemicals were used as received. Deionized water (Milli-Q, 18.25 M $\Omega$ ) was obtained through an EMD Millipore water purification system.

### Synthesis of graphene oxide

Graphene oxide ( $\text{GO}_x$ ) was produced using the improved Hummer method.<sup>24</sup> Firstly, graphite flakes (1.0 g) were mixed with a solution containing concentrated sulfuric acid (120 mL) and phosphoric acid (13.3 mL), and stirred for 1 h at 50 °C. Afterwards,  $\text{KMnO}_4$  (6 g) was slowly added, and the suspension was kept at 50 °C for another 12 h. The solution was then allowed to cooled down to room temperature before poured it into a mixture of cold water (133.3 mL) and 30%  $\text{H}_2\text{O}_2$  (1 mL). The suspension was later centrifuged, the supernatant was decanted, and the remnants were washed sequentially with 10% HCl, DI water (2 $\times$ ), ethanol (2 $\times$ ), and finally with DI water. Each centrifugation process was carried out at 6000 rpm for 2 h. At last, the samples were recovered by freeze drying. Nitrogen doped reduced graphene oxide (N-rGO) was prepared by heating the  $\text{GO}_x$  at 750 °C under ammonia ( $\sim 80.5$  mL min<sup>-1</sup>) and Ar atmosphere ( $\sim 106$  mL min<sup>-1</sup>) for 90 min. A control sample of rGO<sub>x</sub> (without nitrogen) was obtained using instead a mixture of

5%  $\text{H}_2$  and 95% Ar as the reducing atmosphere. Synthesis of Co– $\text{MoS}_2$ @N-rGO<sub>x</sub>.

Typically, 0.0447 g (0.6 mmol) thiourea, 0.0768 g (0.3 mmol) molybdenum hexacarbonyl, and N-rGO<sub>x</sub> (0.0180 g) were dispersed in 10 mL of ethanol. Cobalt nitrate hexahydrate was selected as the dopant precursor. The precursors were dissolved in ethanol using an ultrasonic bath for 1 hour. The cobalt content was calculated with respect to the transition metal content, such that a stoichiometric metal disulfide was maintained. The solutions were then transferred into an oil bath at 90 °C for 20 h to completely evaporate the solvent. The samples were transferred to a quartz chamber located inside the microwave oven (Milestone Pyro) with an adjustable power source of 1200 W operating at 2.65 GHz. An inert atmosphere was created by evacuating the air (15 min) and refilling the chamber with Ar (15 min), this process was repeated two times to minimize sample oxidation. The target product was then achieved by irradiating the precursors at 900 W for 30 s continuously followed by 30 s of cool down, the cycle was repeated 3 times. During the synthesis process, weak sparks could be observed inside the chamber.

### Material characterization

Powder X-ray diffraction (XRD) patterns were collected on a PANalytical X'pert diffractometer (Cu-K $\alpha$ ,  $\lambda = 1.5406$  Å) with 45 kV and 40 mA at ambient temperature, using a continuous mode in the  $2\theta$  angular range of 10° to 80° with a scan speed of 0.0279°·s<sup>-1</sup>. Scanning electron microscopy studies were carried out with a FE-SEM, Carl Zeiss Merlin equipped with energy dispersive X-ray spectroscopy (EDS). Transmission electron microscopy (TEM) images were obtained on FEI Talos L 120C, and the STEM high-angle annular dark-field (HAADF) images were recorded on a Thermo Scientific Themis Z at 300 kV, EDX was acquired using a SuperX EDX detector, and EELS was recorded on a GIF quantum ER spectrometer. Surface elemental composition and valence states were examined by X-ray photoelectron spectroscopy (XPS) using a Kratos Axis Ultra DLD electron-spectrometer equipped with a monochromatic X-ray source (Al K $\alpha$  line of 1486.6 eV), the XPS spectra were calibrated with the C 1s = 284.4 eV (C–C sp<sup>2</sup>).<sup>25,26</sup> Raman spectroscopy was carried out with a Renishaw inVia Raman spectrometer fitted with a diffraction grating of 2400 lines per mm, excited with a radiation of 514 nm Ar-ion laser and calibrated with Si single crystal.

### Electrochemical measurements

The electrochemical catalytic activity was examined in a three-electrode cell using a glassy carbon rotating disc electrode (0.19635 cm<sup>2</sup>) as working electrode, a platinum wire as counter electrode, and a reversible hydrogen electrode (RHE, HydroFlex) as the reference electrode. The ink solution was prepared by mixing 5 mg of catalyst in 900  $\mu\text{L}$  DI-water, 300  $\mu\text{L}$  ethanol, and 50  $\mu\text{L}$  of 0.5 wt% Nafion (Alfa Aesar). After sonication for 1 h, 20  $\mu\text{L}$  ink solution was carefully dropped onto the GCE (loading 0.408 mg cm<sup>-2</sup>) and dried in a vacuum chamber overnight. Prior to the electrochemical measurement, the electrolyte

(0.5 M H<sub>2</sub>SO<sub>4</sub>) was de-gassed by bubbling high purity argon for 15 min. The linear sweep voltammetry (LSV) curves were acquired at a potential scan rate of 10 mV s<sup>-1</sup>. The internal resistance (iR) drop was compensated for 90% in the LSV measurements. Meanwhile, the electrochemical impedance spectroscopy (EIS) was measured at an overpotential of -150 mV (vs. RHE) with frequencies from 10 kHz to 0.1 Hz and an amplitude of 10 mV. The durability test was performed using cyclic voltammetry in the range of -0.15 V to +0.35 V for 5000 cycles at a scan rate of 100 mV s<sup>-1</sup>.

### Computational details

Density functional theory (DFT) calculations with the generalized gradient approximation and the revised Perdew, Burke, and Ernzerhof parametrization<sup>27</sup> were performed using the SIESTA code.<sup>28</sup> The valence electrons were represented by a linear combination of pseudo-atomic numerical orbitals using a double- $\zeta$  polarized basis with an energy shift of 200 meV when determining the cutoff radii.<sup>29</sup> A mesh cutoff of 250 Ry was used to define the real-space grid needed for charge and potential integration, and only the  $\Gamma$ -point of the Brillouin zone was considered. All systems were geometrically optimized until the maximum forces were  $<0.04$  eV·Å<sup>-1</sup>. Periodic boundary conditions were used with a cell size of 75 × 75 × 30 Å to minimize lateral interactions with periodic images. A hexagonal 2H MoS<sub>2</sub> flake with 50% (100%) sulfur coverage in the S-edges (Mo-edges), and a circumdiameter of ~40 Å (459 atoms) was used to evaluate the preferable sites for cobalt doping. The relative formation energy ( $E_{\text{form}}$ ) was evaluated as  $E_{\text{form}} = E_i - E_b$ , where  $E_i$  is the total energy of the doped flake with a Co atom at a site  $i$ , and  $E_b$  is the total energy of the doped flake with the Co atom at

the center representing the bulk-like Co doping, in this way negative  $E_{\text{form}}$  indicate preferred doping positions.

## Results and discussion

### Morphology and structure

During the microwave synthesis process, we used N-rGO<sub>x</sub> as a susceptor and catalyst support, while molybdenum hexacarbonyl and thiourea as transition metal and chalcogen sources, respectively. After the microwave irradiation process, the resulting composite consisted of two-dimensional few-layer MoS<sub>2</sub> firmly attached to the graphene surface, labeled MoS<sub>2</sub>@N-rGO<sub>x</sub>, a schematic of the composite is depicted in Fig. 1a.

For comparison, a control sample without the N-rGO<sub>x</sub> substrate did not show any XRD features (Fig. S1†) corresponding to MoS<sub>2</sub> after similar microwave treatment, highlighting the importance of the N-GO<sub>x</sub> as support and microwave absorber. On the other hand, when pure N-GO<sub>x</sub> was exposed to the microwave treatment, only a slight increase in the (002) peak intensity of the XRD was observed (Fig. S1†), indicating improved crystallinity due to the thermal annealing. Continuing with the MoS<sub>2</sub>@N-GO<sub>x</sub> composite, its crystal structure was confirmed by XRD (Fig. 2) where the diffractogram had broad features corresponding to the semiconductor 2H MoS<sub>2</sub> phase (JCPDS 37-492). This is expected since high temperature processes result in the formation of the stable 2H phase, instead of the 1T or 1T' that is normally achieved in low temperature hydrothermal processes.<sup>30,31</sup> From XRD we see that the feature corresponding to the (002) crystal plane of MoS<sub>2</sub> is located at 14.2° resulting in an interplanar distance of ~6.2 Å, and its full width at half maximum of ~2° indicates an average thickness of 6 MoS<sub>2</sub> layers using the Scherrer formula.<sup>32,33</sup> In addition, the

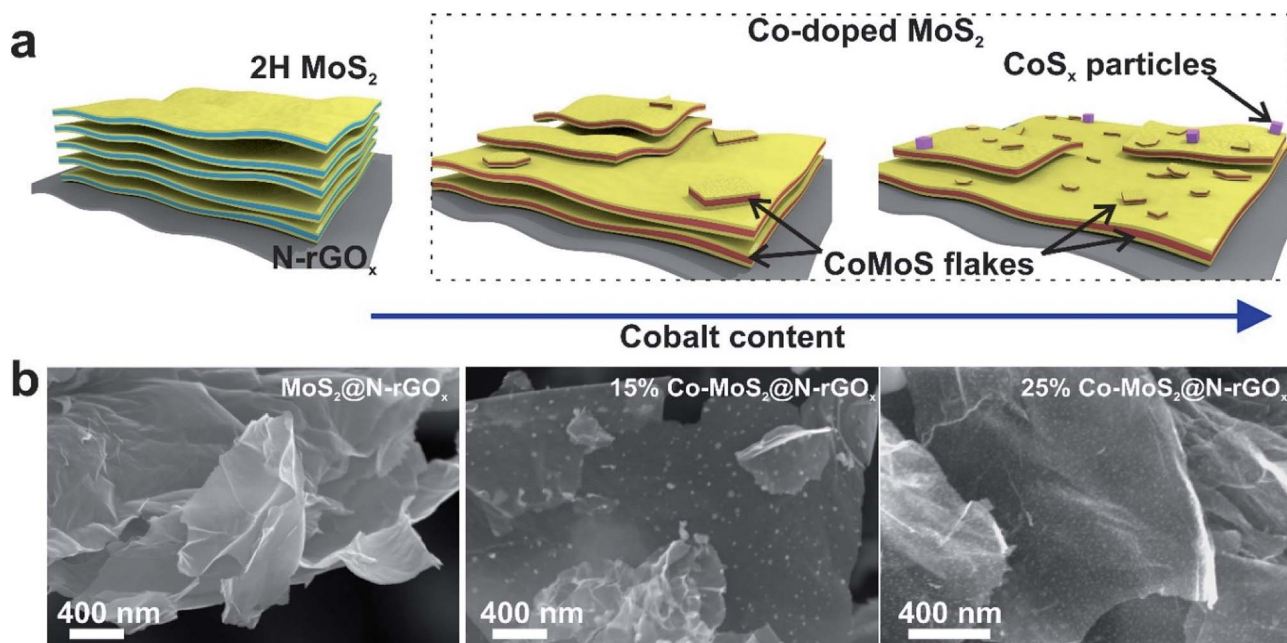


**Fig. 1** (a) Schematic of non-doped and Co-MoS<sub>2</sub>@N-rGO<sub>x</sub>. The Co-MoS<sub>2</sub> exhibit the CoMoS phase (Co atoms mostly located at the edge of MoS<sub>2</sub> flakes), and at higher Co content CoS<sub>x</sub> particles appear. (b) SEM images of non-doped MoS<sub>2</sub>@N-rGO<sub>x</sub>, 15%, and 25% Co-MoS<sub>2</sub>.

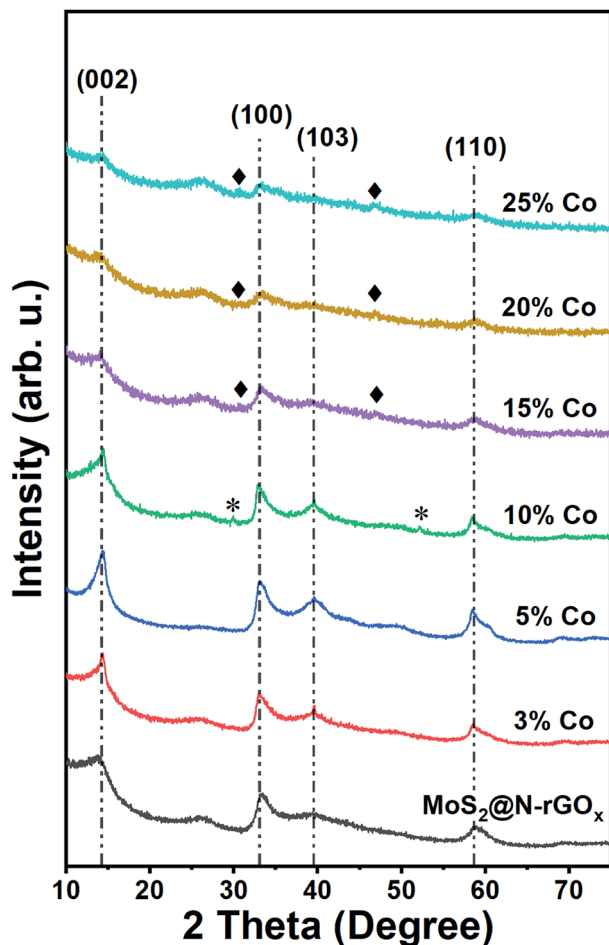


Fig. 2 XRD patterns of pristine and Co–MoS<sub>2</sub>@N-rGO<sub>x</sub>. The vertical lines associated with 2H MoS<sub>2</sub>, peaks associated with cobalt sulfides are marked by \* for features corresponding to Co<sub>9</sub>S<sub>8</sub> and ◆ for Co<sub>1-x</sub>S. The weak peak at 26.0° corresponds to the (002) plane of graphite.

asymmetrical broadening at the low angle side in the (100) and (110) reflections is a feature of turbostratic disordered layered materials.<sup>34,35</sup> The morphology of the as-produced MoS<sub>2</sub> was later studied by SEM and EDS elemental analysis, and we identified the presence and homogeneous distribution of Mo and S (Fig. S2†), but unfortunately no detailed morphological information could be obtained from SEM, and instead only smooth sheets of N-rGO<sub>x</sub> with no clear signs of nanostructured MoS<sub>2</sub> were observed, see for example Fig. 1b and S3.† However, TEM and STEM-HAADF analysis revealed the presence of a MoS<sub>2</sub> coating covering the entire graphene flakes (Fig. 3a–d, and S4, S5†), where the coating follows the overall shape of the graphene flakes suggesting a strong interaction with the substrate. The precise MoS<sub>2</sub> thickness was difficult to evaluate since the layers grouped together in ~3–8 MoS<sub>2</sub> sheets with varying interlayer distance as seen from Fig. 3b–d, in agreement with the XRD. In some regions an average interlayer distance of 6.3 Å was observed, consistent with the (002) plane of 2H MoS<sub>2</sub>. Although the layer separation is slightly larger than the corresponding spacing in molybdenite (6.15 Å), there are larger

variations at other locations due to the irregular nature of the flakes. Overall, these results point towards a highly defective few-layer MoS<sub>2</sub>.

We continued our study with the addition of cobalt nitrate to form Co-doped MoS<sub>2</sub> and investigated the effects of Co concentration in the formation of the CoMoS phase and CoS<sub>x</sub>. We prepared five distinct samples containing 3, 5, 10, 15, and 25 at% of cobalt relative to the metal content. After the microwave treatment, there were no major changes in the diffractogram (Fig. 2) at low cobalt concentration, suggesting that most of the cobalt was properly introduced into the MoS<sub>2</sub> lattice, later identified as the CoMoS phase by Raman and XPS characterization. However, for concentrations above 10 at%, some weak features in the diffractogram appeared, indicating the presence of various cobalt sulfides. In particular, the 10% Co doped sample exhibits two peaks at 29.8° and 52.2° possibly corresponding to Co<sub>9</sub>S<sub>8</sub> (crystal planes (311) and (440), JCPDS 75-2023), and for samples exceeding 15% another two new peaks at 30.6° and 46.8° formed that could be originated from the (100) and (102) planes of Co<sub>1-x</sub>S (JCPDS 42-0826). Nevertheless, the limited information is insufficient to properly identify the nature of the cobalt sulfide, but it suggests the coexistence of cobalt as dopant in MoS<sub>2</sub> and as cobalt sulfide at large Co content. Another consequence of cobalt doping for samples above 15% is the significant reduction in peak intensity of features related to MoS<sub>2</sub>, this of course, can be related to the lower amount of Mo, and thus MoS<sub>2</sub>, but it also suggests the reduction in crystallite size caused by Co due to interruption of the MoS<sub>2</sub> growth. The latter is typically observed in materials containing the CoMoS phase, as more Co occupy the edge sites in MoS<sub>2</sub> limiting the crystal growth along the plane.<sup>9,10,36</sup> The latter is also evidenced from SEM and TEM studies (Fig. 1b, 3e–h and S4†) where small flakes and particles are seen along the surface, in which these flakes gradually decrease in size with increasing amount of cobalt. In addition, we did not observe any significant segregation from EDS elemental mapping (Fig. 3, S6 and Table S1†) regardless of the cobalt doping, meaning that even if CoS<sub>x</sub> particles are formed, these are also homogeneously dispersed in the material. The shelf life of the samples was measured after storing them for 3 months at ambient conditions, and samples with large Co content, particularly ≥20%, exhibited signs of oxidation evidence by the appearance of new diffraction peaks in the XRD patterns (Fig. S7†). The new XRD features suggest the formation of partial oxides such as CoMoS<sub>2.17</sub>O<sub>1.12</sub> (JCPDS 16-0438) and CoMoS<sub>2.96</sub>O<sub>0.25</sub> (JCPDS 16-0105), fortunately, the oxidation process was not seen in other samples. Finally, we want to highlight a peculiar characteristic of samples doped with low Co content (5 and 10 at%), where we found several core-shell nanoparticles, see Fig. S8,† in which the shell is a layered material consistent with MoS<sub>2</sub>, while the core composition is unknown. The particle size was around 15–30 nm and the shell consisted of few MoS<sub>2</sub> layers. These particles were rarely observed and they did not comprise the majority of the sample, complicating its study and characterization, however further optimization could potentially increase the yield allowing to properly investigate the properties of such core-shell particles.

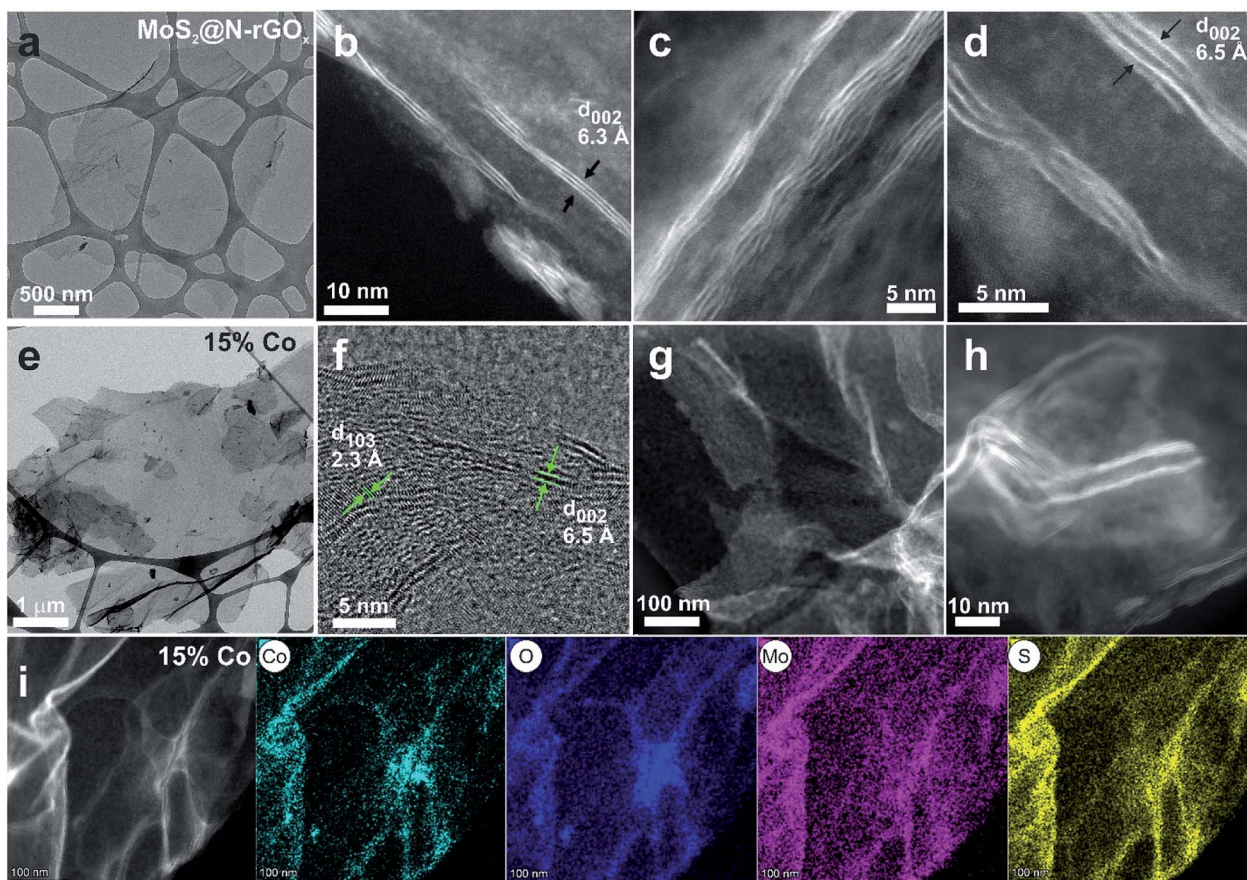


Fig. 3 TEM and STEM-HAADF images of (a–d)  $\text{MoS}_2@\text{N-rGO}_x$ , and (e–h) 15% Co– $\text{MoS}_2@\text{N-rGO}_x$ . (i) STEM-BF image and EDS elemental analysis of 15% Co– $\text{MoS}_2@\text{N-rGO}_x$ .

### Elemental composition and nature of cobalt doping

The evolution of the oxygen content was evaluated at different steps along the synthesis process, and we observed an increase from 2.41 at% for  $\text{N-rGO}_x$  to 8.09 at% for non-doped  $\text{MoS}_2@\text{N-rGO}_x$ , (see XPS survey in Fig. S9 and Table S1†), and then a higher oxygen content was observed at large Co concentration, reaching 11.44 and 13.35 at% for samples with 15% and 25% of cobalt. However, no XRD features of metal oxides were observed, and in addition the oxygen homogeneously distributed along the sample as seen in the elemental mappings in Fig. 3i, S2 and S6†, suggest the formation of oxygenated groups, such as sulfates  $(\text{SO}_4)^{2-}$  as indicated later by XPS. We now focus on the 15% Co– $\text{MoS}_2@\text{N-rGO}_x$  sample and its high resolution XPS spectra shown in Fig. 4. The XPS spectrum of O 1s is composed of three individual peaks at 530.5 eV, 531.7 eV, and 533.3 eV, these could originate from the lattice oxygen in Mo or Co oxides, as well as adsorbed oxygen moieties.<sup>37,38</sup> As the amount of cobalt increases, the overall O 1s peak shifts toward higher energies (Fig. 4c and S10†) indicating a larger contribution from oxygen in metal oxides. On the other hand, large Co content downshifted both Mo 3d and S 2p peaks (Fig. 4 and S10†), as evidenced in Fig. 4a where the binding energies of the Mo 3d<sub>3/2</sub> and 3d<sub>5/2</sub> features corresponding to Mo(IV) (232.0/228.8 eV) are slightly lower than those in  $\text{MoS}_2@\text{N-rGO}_x$  (232.2/

229.0 eV, Fig. S11†). This phenomenon is consistent with the lower effective nuclear charges of Mo and S compared to  $\text{MoS}_2$  corresponding to a reduction of the oxidation state. However, it is still possible to observe two other doublets at 235.3/232.2 eV and 232.9/229.7 eV that indicate the existence of Mo(VI) and Mo(V), respectively, the coexistence of all these features have been reported in materials with mixed sulfides and oxides, such as  $\text{MoO}_x\text{S}_y$ .<sup>39–42</sup> In comparison, the non-doped  $\text{MoS}_2@\text{N-rGO}_x$  exhibits only features corresponding to Mo(IV) and Mo(VI). The deconvolution of S 2p spectra yielded three doublets for the S 2p<sub>3/2</sub> and S 2p<sub>1/2</sub>, the first one (161.6/162.8 eV) is assigned to  $\text{S}_2^-$  in  $\text{MoS}_2$ , the second one (162.9/164.0 eV) to nonstoichiometric  $\text{MoS}_x$ , and the third one (168.2/169.4 eV) with a larger intensity when compared to the non-doped counterpart is related to sulfate moieties such as  $\text{SO}_4^{2-}$ , which is in agreement with the increase in oxygen and cobalt content, probably forming Co and Mo sulfates.<sup>30,31,43,44</sup> For the case of cobalt, the Co 2p spectrum can be resolved into two spin-orbit doublets and four satellites. The first doublet located at 778.8/793.7 eV is attributed to cobalt sulfides, while the doublet at 781.4/796.9 eV and all four satellites correspond to oxidized  $\text{Co}^{2+}/\text{Co}^{3+}$ ,<sup>45,46</sup> the latter increase in intensity only for samples with at least 15% Co, suggesting that at low Co content the vast majority is in the form of sulfides. All Co doped samples have a peak around 778.8 eV, that is close in

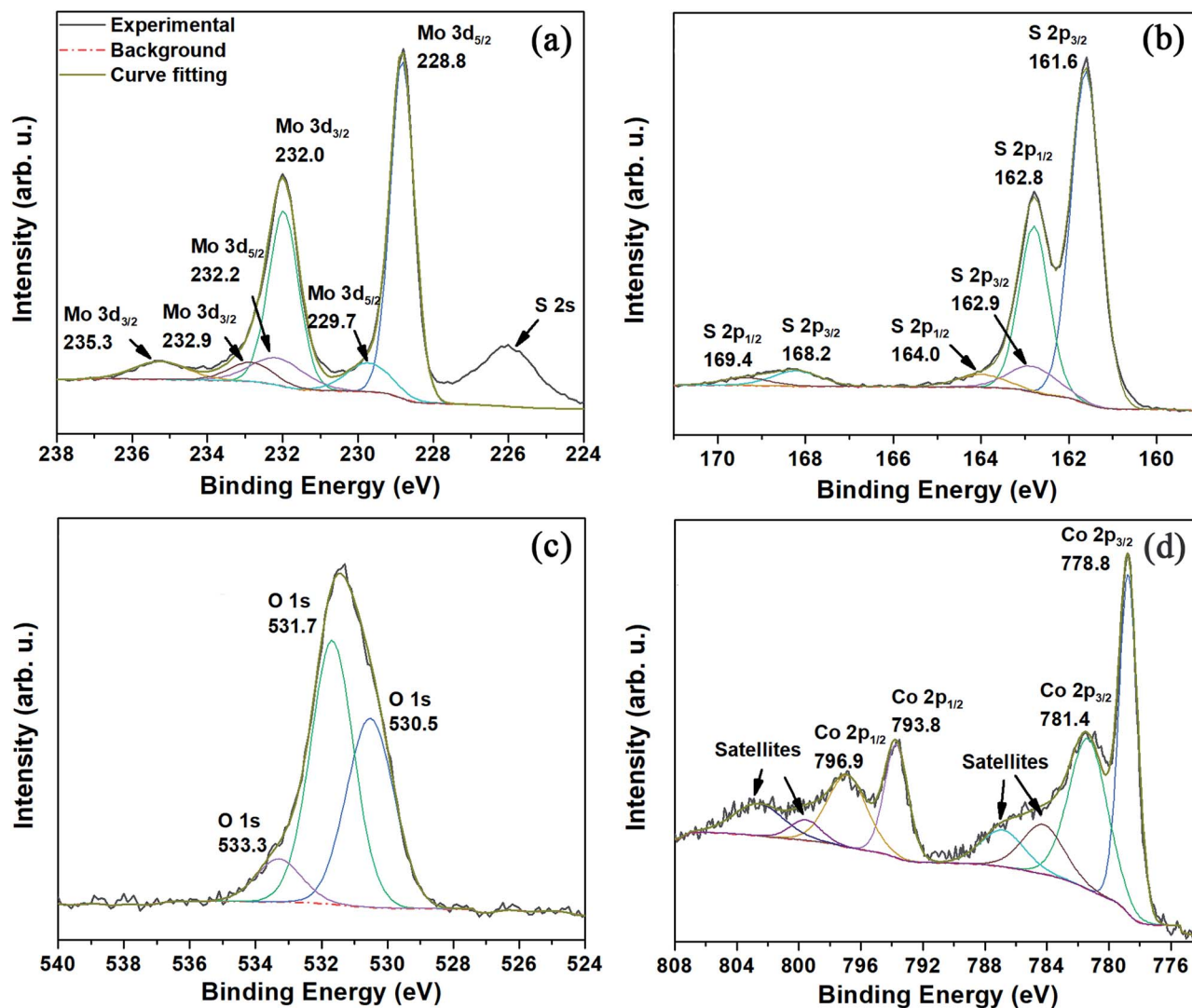


Fig. 4 XPS spectra of (a) Mo 3d, (b) S 2p, (c) O 1s, and (d) Co 2p for the 15% Co-MoS<sub>2</sub>@N-rGO<sub>x</sub>. Detailed information can be found in the main text.

binding energy to those observed in Co<sub>9</sub>S<sub>8</sub>,<sup>47</sup> Co<sub>1-x</sub>S,<sup>48</sup> and the CoMoS phase.<sup>49</sup> We used the binding energy difference as proposed by Alstrup and coworkers<sup>13,49</sup> to better understand the nature of cobalt doping. This method involves evaluating two binding energy differences  $\Delta E_1$  and  $\Delta E_2$ , defined as  $E(\text{Co } 2p_{3/2}) - E(\text{S } 2p_{3/2})$ , and  $E(\text{Mo } 3d_{5/2}) - E(\text{S } 2p_{3/2})$ , respectively. In our case, we found  $\Delta E_1 = 617.2$  eV and  $\Delta E_2 = 67.2$  eV, which are in agreement with previously reported values for the CoMoS phase ( $\Delta E_1 = 617.0\text{--}616.0$  eV,  $\Delta E_2 = 66.9\text{--}65.9$  eV),<sup>13,50</sup> indicating that the major contributing phase is CoMoS.

We used Raman spectroscopy to identify changes in the N-rGO<sub>x</sub> substrate as well as the 2H MoS<sub>2</sub> caused by the addition of cobalt, initially we noticed that the ratio of the D and G bands ( $I_D/I_G$ ) in graphene increased from 0.81 for rGO<sub>x</sub> (reduced under Ar/H<sub>2</sub> at 750 °C) to 0.88 and then to 0.96 for N-rGO<sub>x</sub> and non-doped MoS<sub>2</sub>@N-rGO<sub>x</sub> respectively, see Fig. S12.† Indicating that in each subsequent process the graphitic lattice is disrupted, first by the nitrogen introduction, and then due to the

decoration with MoS<sub>2</sub>, reinforcing the idea of a strong interaction within the metal chalcogenide and the substrate. The Raman spectra for the active region of MoS<sub>2</sub> is depicted in Fig. 5. The two peaks located at 379.9 cm<sup>-1</sup> and 405.3 cm<sup>-1</sup> correspond to the in-plane E<sub>2g</sub><sup>1</sup> and out-of-plane A<sub>1g</sub> vibrational modes of the 2H MoS<sub>2</sub>. Both E<sub>2g</sub><sup>1</sup> and A<sub>1g</sub> features are red-shifted in comparison to bulk MoS<sub>2</sub> (383 and 408 cm<sup>-1</sup>), similar red-shift has been observed in the presence of biaxial strain on free-standing MoS<sub>2</sub> sheets.<sup>51</sup> In our case, the abundance of defects and dopants could cause the biaxial strain and thus the observed shift. Additionally, Raman spectroscopy also indicates the abundance of edge-terminated structures as seen by the E<sub>2g</sub><sup>1</sup>/A<sub>1g</sub> integrated intensity ratio of ~0.5 as expected for the CoMoS phase, since the A<sub>1g</sub> (E<sub>2g</sub><sup>1</sup>) mode is preferentially excited for edge-(terrace)-terminated layers,<sup>52,53</sup> and so the Co-doped MoS<sub>2</sub>@N-rGO<sub>x</sub> exhibit, in general, large number of electrocatalytically active sites.

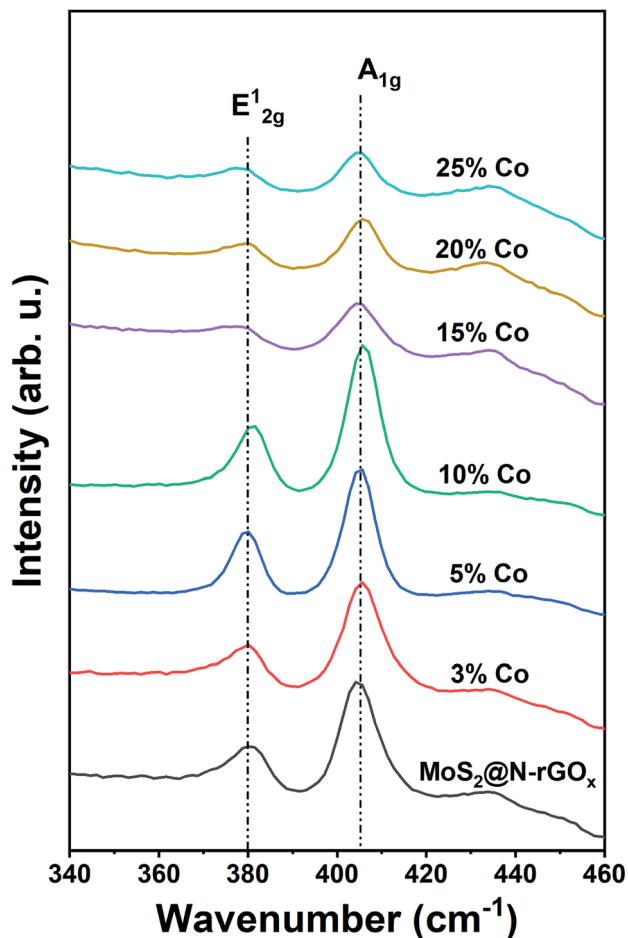


Fig. 5 Raman spectra of non-doped and Co-doped  $\text{MoS}_2@N\text{-rGO}_x$ .

We also performed *ab initio* theoretical calculations to investigate the preferential doping sites of cobalt on a 2H  $\text{MoS}_2$  flake, we replaced individual Mo atoms by Co and then evaluated the relative formation energy ( $E_{\text{form}}$ ) to identify stable doping configurations. The results are shown in Fig. 6 as a 2D map of the hexagonal  $\text{MoS}_2$  flake indicating the doping sites, while the color specifies the calculated  $E_{\text{form}}$  with negative values indicating preferable configurations. From the observed  $E_{\text{form}}$  is easier to understand the formation of the  $\text{CoMoS}$  phase, as Co will preferentially occupy the edge sites of  $\text{MoS}_2$  sheets with vertices being the most stable sites with  $E_{\text{form}}$  of around  $-3.5$  eV, followed by both Mo- and S-edges ( $-3.0$  to  $-1.5$  eV). It is also clear that the  $E_{\text{form}}$  weakens significantly up to  $-0.5$  eV (seen as green) for the first neighbors after the edge atoms, and then  $E_{\text{form}}$  is further reduced to values close to zero (relative to the bulk-like Co-doping energy) for the second neighbors and so on. These results have two main consequences, the first one being that Co will mostly occupy the Mo-sites at vertices and edges, and the second one that it will limit the crystal growth of  $\text{MoS}_2$  flakes exposing additional edge atoms.

### Hydrogen evolution performance

The hydrogen evolution reaction was investigated in acidic electrolyte ( $0.5$  M  $\text{H}_2\text{SO}_4$ ) using linear sweep voltammetry (LSV)

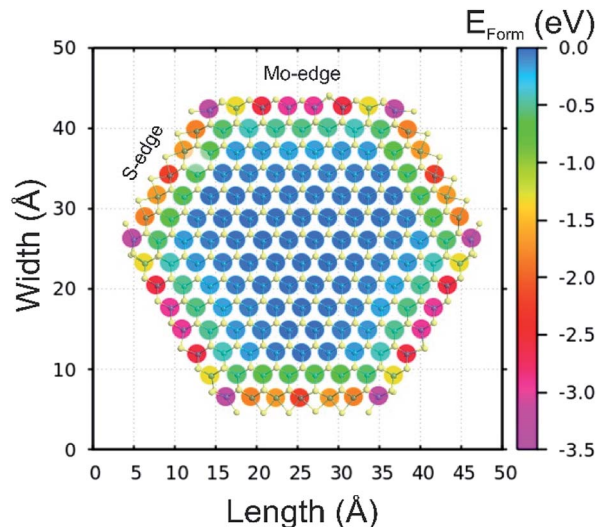


Fig. 6 Relative formation energy ( $E_{\text{form}}$ ) of cobalt atoms occupying diverse Mo sites along a single 2H  $\text{MoS}_2$  flake. The S-edges (Mo-edges) were passivated at 50% (100%). Negative values of  $E_{\text{form}}$  indicate preferable sites for cobalt doping.

in a three-electrode cell, the iR-compensated data is shown in Fig. 7. From the LSV studies, it is clear that all the Co-doped samples exhibited a smaller onset potential for HER catalysis than that of pristine  $\text{MoS}_2@N\text{-rGO}_x$ . It is also evident that there is a gradual improvement in the HER activity with increased amount of Co reaching a maximum at 15%. At larger Co concentration, the HER activity (measured as the overpotential to achieve  $10$  mA  $\text{cm}^{-2}$ ,  $\eta_{10}$ ) stalls, and a slight deterioration is observed. The resulting  $\eta_{10}$  is reduced from  $238$  mV for the non-doped  $\text{MoS}_2@N\text{-GO}_x$  to  $197$  mV for the 15% Co- $\text{MoS}_2@N\text{-GO}_x$ , in agreement with previous CoMoS materials.<sup>9,10</sup> The Tafel slope was evaluated by performing a linear fitting at the low current density region and it was found that non-doped and Co- $\text{MoS}_2@N\text{-GO}_x$  exhibit similar Tafel slopes of  $61$  mV  $\text{dec}^{-1}$ , indicating that in our case Co doping mainly decreased the onset potential and has little effect on the HER mechanism. The observed Tafel slope suggests that the HER occurs *via* the Volmer–Heyrovský mechanism where the adsorption of protons dominates the kinetics. Considering the fast synthesis process, our best sample exhibit comparable performance with other  $\text{MoS}_2$ -based catalysts produced, for example, *via* solvothermal, exfoliation, or annealing methods, a detailed comparison is included in Table S2.† Electrochemical impedance spectroscopy studies prove that cobalt doping reduces the charge transfer resistance (Fig. 7c) from  $55.2$   $\Omega$   $\text{cm}^2$  to  $17.1$   $\Omega$   $\text{cm}^2$  for pristine and 15% Co-doped samples, respectively. The lower charge transfer resistance is attributed to the destabilization (reduced binding energy) of the Mo 3d orbital with increase Co content (Fig. S10a†), and thus improving the interaction with the  $N\text{-rGO}_x$  substrate and facilitating the electron transport. The stability of the 15% Co- $\text{MoS}_2@N\text{-GO}_x$  electrocatalyst was investigated by cyclic voltammetry (CV) by performing 5000 CV cycles within the range  $-0.15$  V to  $+0.35$  V (*vs.* RHE) at a scan rate of  $100$  mV  $\text{s}^{-1}$ . Fig. 7d depicts the initial and final polarization curves where no obvious degradation was observed.

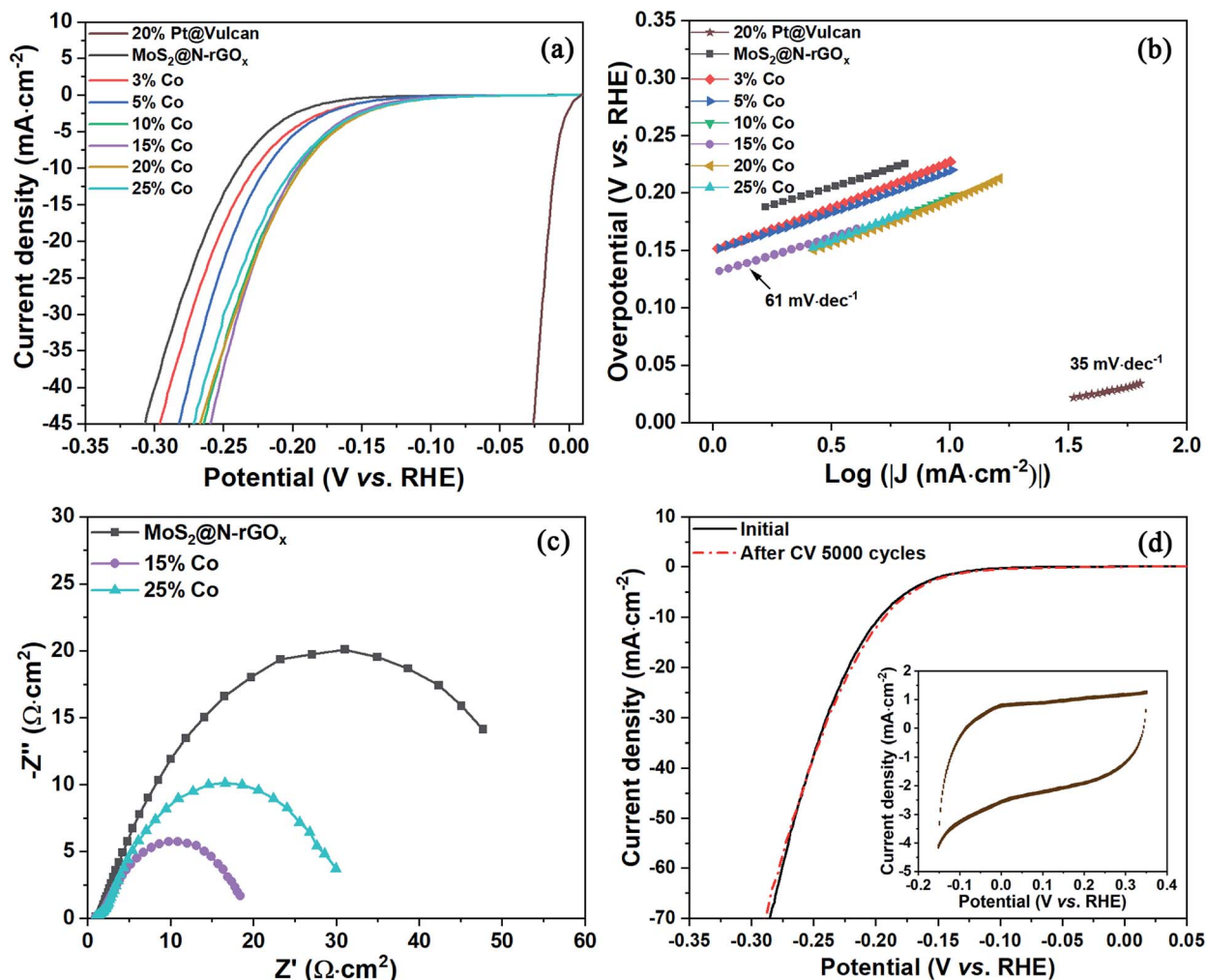


Fig. 7 (a) Polarization curves of non-doped and Co–MoS<sub>2</sub>@N-rGO<sub>x</sub>, and 20% Pt@Vulcan (with iR compensation), (b) the corresponding Tafel plots. (c) Electrochemical impedance spectroscopy of MoS<sub>2</sub>@N-rGO<sub>x</sub>, 15% and 25% Co–MoS<sub>2</sub>@N-rGO<sub>x</sub> in 0.5 M H<sub>2</sub>SO<sub>4</sub> at an overpotential of 150 mV, inset is the equivalent circuit. (d) Polarization curves of 15% Co–MoS<sub>2</sub>@N-rGO<sub>x</sub> before and after the durability test, the inset shows the 5000 CV cycles in the range of –0.15 to +0.35 V (vs. RHE).

## Conclusions

Two-dimensional few-layers MoS<sub>2</sub> with a 2H crystal structure was grown directly on N-rGO<sub>x</sub> through a solid-state reaction using microwave irradiation lasting only 2 minutes. The as-produced MoS<sub>2</sub> was 3–8 layer thick with a turbostratic distribution, and the addition of cobalt results in the formation of the CoMoS phase where few-layer Co–MoS<sub>2</sub> nanosheets also cover the entire N-rGO<sub>x</sub> substrate. The presence of Co hinders the growth of fully continuous MoS<sub>2</sub> layers, and thus the Co–MoS<sub>2</sub> nanosheets are dominated by edge-terminated structures, leading to a high proportion of active site exposure and promoting efficient electron transfer. The HER activity was significantly improved for the 15% Co–MoS<sub>2</sub>@N-rGO<sub>x</sub> with a relatively low overpotential of 197 mV at 10 mA cm<sup>–2</sup> and a Tafel slope of 61 mV dec<sup>–1</sup>. The catalyst also possessed good operational stability with no apparent degradation after 5000 CV cycles. In addition, as an effective synthesis technique,

microwave irradiation is expected to play a more important role in the research of novel materials.

## Conflicts of interest

There are no conflicts to declare.

## Acknowledgements

E. G. E. and S.K. acknowledge support from the Swedish Research Council (2018-03937, 2019-05114) and the Olle Engkvist Foundation (186-0637). The authors acknowledge Umeå Core Facility for Electron Microscopy (UCEM) and the Vibrational Spectroscopy Core Facility (ViSp) at Umeå University, Chemical Biological Centre (KBC). Andrey Shchukarev and Andras Gorzsas at Umeå University, KBC, are acknowledged for the assistance with XPS and Raman measurements, respectively. The theoretical simulations were performed on resources provided by the Swedish National Infrastructure for Computing



(SNIC) at the High Performance Computing Center North (HPC2N).

## References

- 1 M. A. Lukowski, A. S. Daniel, F. Meng, A. Forticaux, L. Li and S. Jin, *J. Am. Chem. Soc.*, 2013, **135**, 10274–10277.
- 2 J. Tang, M. Sakamoto, H. Ohta and K. Saitow, *Nanoscale*, 2020, **12**, 4352–4358.
- 3 J. Hu, B. Huang, C. Zhang, Z. Wang, Y. An, D. Zhou, H. Lin, M. K. H. Leung and S. Yang, *Energy Environ. Sci.*, 2017, **10**, 593–603.
- 4 X. Hai, W. Zhou, S. Wang, H. Pang, K. Chang, F. Ichihara and J. Ye, *Nano Energy*, 2017, **39**, 409–417.
- 5 T. Huang, J. Xu and Y. Fan, *Appl. Catal., B*, 2018, **220**, 42–56.
- 6 Y. Wu, M. Zarei-Chaleshtori, B. Torres, T. Akter, C. Diaz-Moreno, G. B. Saupe, J. A. Lopez, R. R. Chianelli and D. Villagrán, *Int. J. Hydrogen Energy*, 2017, **42**, 20669–20676.
- 7 X. Hong, K. Chan, C. Tsai and J. K. Nørskov, *ACS Catal.*, 2016, **6**, 4428–4437.
- 8 P. Li, Y. Yang, S. Gong, F. Lv, W. Wang, Y. Li, M. Luo, Y. Xing, Q. Wang and S. Guo, *Nano Res.*, 2019, **12**, 2218–2223.
- 9 S. S. Grønberg, M. Šarić, P. G. Moses, J. Rossmeisl and J. V. Lauritsen, *J. Catal.*, 2016, **344**, 121–128.
- 10 X. Dai, K. Du, Z. Li, M. Liu, Y. Ma, H. Sun, X. Zhang and Y. Yang, *ACS Appl. Mater. Interfaces*, 2015, **7**, 27242–27253.
- 11 A. M. de Jong, V. H. J. (San) de Beer, J. A. Rob van Veen and J. W. (Hans) Niemantsverdriet, *J. Vac. Sci. Technol., A*, 1997, **15**, 1592–1596.
- 12 N. Zhang, W. Ma, F. Jia, T. Wu, D. Han and L. Niu, *Int. J. Hydrogen Energy*, 2016, **41**, 3811–3819.
- 13 R. Bose, Z. Jin, S. Shin, S. Kim, S. Lee and Y.-S. Min, *Langmuir*, 2017, **33**, 5628–5635.
- 14 J. Deng, H. Li, J. Xiao, Y. Tu, D. Deng, H. Yang, H. Tian, J. Li, P. Ren and X. Bao, *Energy Environ. Sci.*, 2015, **8**, 1594–1601.
- 15 D. Vollath and D. V. Szabó, *Mater. Lett.*, 1998, **35**, 236–244.
- 16 D. H. Youn, J. W. Jang, J. Y. Kim, J. S. Jang, S. H. Choi and J. S. Lee, *Sci. Rep.*, 2014, **4**, 1–8.
- 17 S. Balaji, D. Mutharasu, N. Sankara Subramanian and K. Ramanathan, *Ionics*, 2009, **15**, 765–777.
- 18 K. Z. Du, A. Chaturvedi, X. Z. Wang, Y. Zhao, K. K. Zhang, M. Iqbal Bakti Utama, P. Hu, H. Jiang, Q. H. Xiong and C. Kloc, *Dalton Trans.*, 2015, **44**, 13444–13449.
- 19 H. J. Kitchen, S. R. Vallance, J. L. Kennedy, N. Tapia-Ruiz, L. Carassiti, A. Harrison, A. G. Whittaker, T. D. Drysdale, S. W. Kingman and D. H. Gregory, *Chem. Rev.*, 2014, **114**, 1170–1206.
- 20 R. Sandström, E. Gracia-Espino, G. Hu, A. Shchukarev, J. Ma and T. Wågberg, *Nano Energy*, 2018, **46**, 141–149.
- 21 H. Shen, E. Gracia-Espino, L. Wang, D. Qin, S. Gao, X. Mamat, W. Ren, T. Wågberg and G. Hu, *Electrochem. Commun.*, 2017, **81**, 116–119.
- 22 R. Sandström, J. Ekspong, E. Gracia-Espino and T. Wågberg, *RSC Adv.*, 2019, **9**, 17979–17987.
- 23 M. H. Suliman, A. Adam, M. N. Siddiqui, Z. H. Yamani and M. Qamar, *Carbon*, 2019, **144**, 764–771.
- 24 D. C. Marcano, D. V. Kosynkin, J. M. Berlin, A. Sinitskii, Z. Sun, A. Slesarev, L. B. Alemany, W. Lu and J. M. Tour, *ACS Nano*, 2010, **4**, 4806–4814.
- 25 G. Speranza, L. Minati and M. Anderle, *J. Appl. Phys.*, 2007, **102**, 043504.
- 26 P. R. Kidambi, B. C. Bayer, R. Blume, Z.-J. Wang, C. Baetz, R. S. Weatherup, M.-G. Willinger, R. Schloegl and S. Hofmann, *Nano Lett.*, 2013, **13**, 4769–4778.
- 27 B. Hammer, L. B. Hansen and J. K. Nørskov, *Phys. Rev. B*, 1999, **59**, 7413–7421.
- 28 J. M. Soler, E. Artacho, J. D. Gale, A. García, J. Junquera, P. Ordejón and D. Sánchez-Portal, *J. Phys.: Condens. Matter*, 2002, **14**, 2745–2779.
- 29 J. Junquera, Ó. Paz, D. Sánchez-Portal and E. Artacho, *Phys. Rev. B*, 2001, **64**, 235111.
- 30 J. Ekspong, R. Sandström, L. P. Rajukumar, M. Terrones, T. Wågberg and E. Gracia-Espino, *Adv. Funct. Mater.*, 2018, **28**, 1802744.
- 31 J. Ekspong, T. Sharifi, A. Shchukarev, A. Klechikov, T. Wågberg and E. Gracia-Espino, *Adv. Funct. Mater.*, 2016, **26**, 6766–6776.
- 32 S. Iqbal, Z. Pan and K. Zhou, *Nanoscale*, 2017, **9**, 6638–6642.
- 33 K. Chang, M. Li, T. Wang, S. Ouyang, P. Li, L. Liu and J. Ye, *Adv. Energy Mater.*, 2015, **5**, 1402279.
- 34 M. Poisot, W. Bensch, S. Fuentes, C. Ornelas and G. Alonso, *Catal. Lett.*, 2007, **117**, 43–52.
- 35 D. L. Bish and J. E. Post, *Modern Powder Diffraction*, De Gruyter, Berlin, Boston, 1989.
- 36 H. Topsøe, B. S. Clausen, R. Candia, C. Wivel and S. Mørup, *J. Catal.*, 1981, **68**, 433–452.
- 37 R. D. Nikam, P. A. Sonawane, R. Sankar and Y. T. Chen, *Nano Energy*, 2017, **32**, 454–462.
- 38 L. Stobinski, B. Lesiak, A. Malolepszy, M. Mazurkiewicz, B. Mierzwa, J. Zemek, P. Jiricek and I. Bielloshapka, *J. Electron Spectrosc. Relat. Phenom.*, 2014, **195**, 145–154.
- 39 X. Shao, J. Tian, Q. Xue and C. Ma, *J. Mater. Chem.*, 2003, **13**, 631–633.
- 40 J. Qiu, Z. Yang and Y. Li, *J. Mater. Chem. A*, 2015, **3**, 24245–24253.
- 41 L. Benoist, D. Gonbeau, G. Pfister-Guillouzo, E. Schmidt, G. Meunier and A. Levasseur, *Solid State Ionics*, 1995, **76**, 81–89.
- 42 N. Salazar, I. Beinik and J. V. Lauritsen, *Phys. Chem. Chem. Phys.*, 2017, **19**, 14020–14029.
- 43 J. Dolinska, A. Chidambaram, W. Adamkiewicz, M. Estili, W. Lisowski, M. Iwan, B. Palys, E. J. R. Sudholter, F. Marken, M. Opallo and L. Rassaei, *J. Mater. Chem. B*, 2016, **4**, 1448–1457.
- 44 N. Liu, J. Baek, S. M. Kim, S. Hong, Y. K. Hong, Y. S. Kim, H. S. Kim, S. Kim and J. Park, *ACS Appl. Mater. Interfaces*, 2017, **9**, 42943–42950.
- 45 B. Liu, S. Wei, Y. Xing, D. Liu, Z. Shi, X. Liu, X. Sun, S. Hou and Z. Su, *Chem.–Eur. J.*, 2010, **16**, 6625–6631.
- 46 H. Lin, H. Li, Y. Li, J. Liu, X. Wang and L. Wang, *J. Mater. Chem. A*, 2017, **5**, 25410–25419.
- 47 X. Zheng, J. Guo, Y. Shi, F. Xiong, W.-H. Zhang, T. Ma and C. Li, *Chem. Commun.*, 2013, **49**, 9645.

- 48 C. Dong, L. Guo, Y. He, L. Shang, Y. Qian and L. Xu, *Nanoscale*, 2018, **10**, 2804–2811.
- 49 I. Alstrup, I. Chorkendorff, R. Candia, B. S. Clausen and H. Topsøe, *J. Catal.*, 1982, **77**, 397–409.
- 50 H. Zhang, Y. Li, T. Xu, J. Wang, Z. Huo, P. Wan and X. Sun, *J. Mater. Chem. A*, 2015, **3**, 15020–15023.
- 51 N. Scheuschner, O. Ochedowski, A.-M. Kaulitz, R. Gillen, M. Schleberger and J. Maultzsch, *Phys. Rev. B: Condens. Matter Mater. Phys.*, 2014, **89**, 125406.
- 52 J. L. Verble and T. J. Wieting, *Phys. Rev. Lett.*, 1970, **25**, 362–365.
- 53 D. Kong, H. Wang, J. J. Cha, M. Pasta, K. J. Koski, J. Yao and Y. Cui, *Nano Lett.*, 2013, **13**, 1341–1347.